12

Inherited Crustal Features and Southern Alaska Tectonic History Constrained by Sp Receiver Functions

Michael Everett Mann[1], Karen M. Fischer[1], and Jeffrey A. Benowitz[2]

ABSTRACT

Southern Alaska is a collage of accreted terranes. The deformation history of accreted terranes and the geometric history of their bounding faults reflect both inherited features and associated convergent margin events. We employ S-to-P receiver functions on multiple dense (<20 km spacing) arrays of broadband seismometers across southern Alaska to investigate signals of dynamic tectonic activity. An inboard-dipping (~15°) boundary is imaged aligning with the trace of the Border Ranges Fault, which is interpreted as an unrotated inboard-dipping paleo-subduction (Mesozoic) interface. This observation, along with previous seismic imaging of the Border Ranges Fault and the next outboard terrane-bounding fault, the Contact Fault, buttresses a known history of convergent tectonics that varies along the margin. Large (>10 km) crustal thickness offsets imaged across both the Denali Fault system and the Eureka Creek Fault support a Mesozoic-to-Present inboard-dipping (east and northward) subduction polarity in the region. Additionally, our imaging reveals a significant velocity increase with depth at ~25 km beneath the Copper River Basin, which we interpret as the top of a region of active underplating and/or intrusion of basaltic magmatism. This feature may be related to the generation of a new Wrangell Volcanic Field volcano, resulting from the underlying tear in the subducting slab.

12.1. INTRODUCTION

Continental crust is a palimpsest of tectonic activity, where ancient terrane boundaries and convergent margin structures can persist for tens of millions of years (e.g., Hopper et al., 2017; Li et al., 2020; Long et al., 2019). Thus, imaging crustal architecture can help piece together the inherited and deformation history of a region (e.g., Fuis et al., 2008; Korja & Heikkinen, 2008). Southern Alaska has been a convergent margin since at least the Jurassic, leading to a tectonic quilt of Mezo-Cenozoic tectonostratigraphic accreted terranes (e.g., Nokleberg et al., 1985; Plafker & Berg, 1994). Furthermore, because of successive periods of crustal-scale strike-slip faulting parallel to the western North America margin and dissecting southern Alaska, these accreted terranes have been transported large distances (>1,000 km) along the margin of western North America through time (e.g., Tikoff et al., 2023). Hence, the region is a prime location to investigate inherited versus developed tectonic features, how structural architecture can be preserved through subsequent accretion events, and how these processes are expressed in seismic velocity structure.

Teleseismic scattered-wave imaging has been used for decades to investigate the crustal structure of southern Alaska (e.g., Ferris et al., 2003; Gama et al., 2022a; Kim et al., 2014; Mann et al., 2022; Miller et al., 2018; Rondenay et al., 2008; Zhang et al., 2019). Body waves incident on velocity gradients, such as the Moho, generate scattered waves that can be extracted from within the P-coda (for incident P waves) or preceding the S-wave

[1]*Department of Earth, Environmental and Planetary Sciences, Brown University, Providence, RI, USA*

[2]*Department of Geological Sciences, University of Colorado Boulder, Boulder, CO, USA*

Tectonics and Seismic Structure of Alaska and Northwestern Canada: EarthScope and Beyond, Geophysical Monograph 290, First Edition. Edited by Natalia A. Ruppert, Margarete A. Jadamec, and Jeffrey T. Freymueller.

DOI: 10.1002/9781394195947.ch12
Companion website: www.wiley.com/go/Ruppert

arrival (for incident S waves) through deconvolution, resulting in receiver functions (RFs; e.g., Farra & Vinnik, 2000; Langston, 1977). Analysis of these S-to-P scattered phases as measured in RFs (i.e., Sp RFs) has often been aimed at subhorizontal Moho and lithospheric discontinuities (e.g., Gama et al., 2022a; Lekić et al., 2011), although Sp RFs have also been used to image dipping modern and paleo structural features, for example, in subduction zones (e.g., Kawakatsu et al., 2009; Kumar & Kawakatsu, 2011).

For this study, a recently developed Sp RF common conversion point (CCP) stacking imaging procedure (Hua et al., 2020a) was applied to teleseismic S waves recorded on dense seismometer arrays across southern Alaska (Figure 12.1). This Sp CCP volume reveals inboard-dipping features extending to depth from the surface trace of the Border Ranges Fault (BRF) system that are potentially associated with the Mesozoic paleo-subduction zone when a subduction interface was located along the BRF (e.g., Trop & Ridgway, 2007).

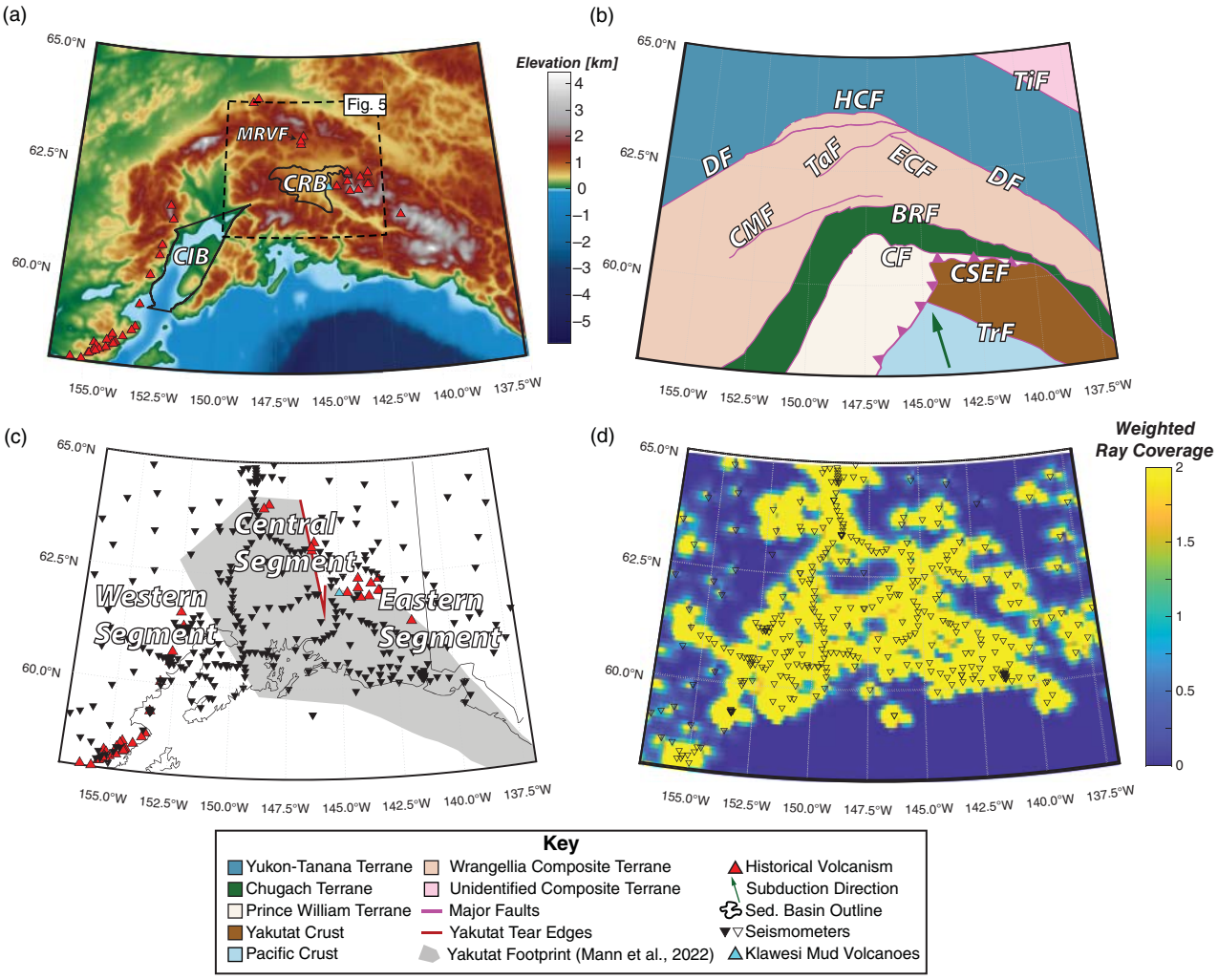

Figure 12.1 Overview of the study area. (a) Topographic map of the study region showing volcanoes and two major sedimentary basins discussed in the text. CIB, Cook Inlet Basin; CRB, Copper River Basin; MRVF, Maclaren River Volcanic Field (Brueseke et al., 2023). The outline of Figure 12.5 is depicted with dashed black lines. (b) Terrane map of the study region showing major faults. TiF, Tintina Fault; DF, Denali Fault; HCF, Hines Creek Fault; TaF, Talkeetna Fault; CMF, Castle Mountain Fault; BRF, Border Ranges Fault; CF, Contact Fault; CSEF, Chugach–St. Elias Fault; TrF, Transition Fault; ECF, Eureka Creek Fault. (c) Location of seismic stations used in this study. The outline of Yakutat oceanic plateau is shown with shaded gray, with tear highlighted in dark red. Approximate delineation of three segments (i.e., western, central, and eastern) is shown. (d) Weighted ray coverage at 50 km depth in the Sp CCP volume. We only interpret along cross sections where the weighted ray coverage is greater than 0.4.

We integrate our new results with previous seismic imaging work on the BRF and Contact Fault (e.g., Fuis et al., 1991; Stephens et al., 1990; Ye et al., 1997) to investigate along-strike variations in paleo-subduction interface preservation and modification (e.g., its rotation toward vertical dip), as well as linked contractional histories. Sharp Moho offsets across terrane-bounding faults including the Denali Fault and Eureka Creek Fault are also imaged. Additionally, the Sp CCP volume reveals a 100 km × 50 km sized positive velocity gradient (PVG) with depth at ~25 km depth beneath the Copper River Basin. Combined with recent seismic analyses across the region, this mid-crustal discontinuity coincides with a dense cluster of earthquakes and may represent active underplating and/or intrusion of basaltic magmatism into the lower crust, rising from a tear in the subducting Yakutat slab that is located directly beneath this discontinuity (Brueseke et al., 2023; Mann et al., 2022).

12.2. GEOLOGIC BACKGROUND

The accretion of the Wrangellia composite terrane (WCT) to North American affinity crust was the largest addition of crust to the continent in the last 200 million years (Trop & Ridgway, 2007). The generally accepted model is that the WCT, primarily oceanic plateau crust (Greene et al., 2010), collided along North America's western (east-dipping) subduction margin at around ca. 100 Ma and then was translated >2,000 km north along margin-parallel strike-slip fault systems (e.g., Tikoff et al., 2023). The Alaska Range suture zone (Ridgway et al., 2002; Trop et al., 2019) is the suture region between the WCT and rocks of North American affinity to the north (Figure 12.1). The Denali Fault system (Amand, 1957) delineates the northern boundary of the Alaska Range suture zone (Trop et al., 2019, 2020), and the Talkeetna Fault delineates the southern boundary of the Alaska Range suture zone (Brennan et al., 2011).

By ca. 50 Ma, the Chugach–Prince William Terrane had been translated north and accreted into place south of the BRF of southern Alaska (Figure 12.1; Cowan, 2003; Freeland & Dietz, 1973; Garver & Davidson, 2015; MacKevett & Plafker, 1974). The Contact Fault delineates the suture between the Chugach and Prince William Terranes (Fisher & Magoon, 1978; Nilsen & Zuffa, 1982). Both the BRF and Contact Fault were likely originally subduction megathrusts that later experienced strike-slip motion (Bol & Roeske, 1993; Brocher et al., 1994; Bruhn et al., 2004; Fuis et al., 1991; Plafker et al., 1989; Trop & Ridgway, 2007). The BRF system has experienced at least ~700 km of slip between ca. 58 and 50 Ma (Smart et al., 1996) playing a role in the northward translation of the Chugach–Prince William Terrane, whereas the Contact Fault experienced an undetermined amount of strike-slip motion during the Eocene and during more recent times (e.g., Bol & Roeske, 1993; Chapman et al., 2012).

The most recent accretion event affecting southern Alaska involves the Yakutat microplate which is a buoyant oceanic plateau with between 11-km (northern subducted leading edge) and 30-km-thick crust (south–east outboard segment) (e.g., Christeson et al., 2010; Eberhart-Phillips et al., 2006; Mann et al., 2022; Rondenay et al., 2008; Worthington et al., 2012). Crustal thickness also varies west (~17 km) to east (~30 km) (Figure 12.3; Worthington et al., 2012).

The Wrangell Arc is linked to the initiation of shallow-slab subduction of the Yakutat oceanic plateau (ca. 30 Ma; Brueseke et al., 2019). The arrival of the Yakutat slab at Alaska's southern convergent margin is also associated with deformation and mountain building across much of southern Alaska (Abers, 2008; Arkle et al., 2013; Benowitz et al., 2019; Enkelmann et al., 2010; Terhune et al., 2019).

The Neogene Yakutat "flat" slab subduction (Enkelmann et al., 2010; Eberhart-Phillips et al., 2006; Pavlis et al., 2004) and true Yakutat collision (Brueseke et al., 2023; Gulick et al., 2007) have also had a profound impact on the evolving structural configuration of the St. Elias syntaxis region (eastern segment) (Figure 12.1c; e.g., Enkelmann et al., 2015a; Jadamec et al., 2013; Koons et al., 2010; Spotila & Berger, 2010). During the last ~3 Ma, faults with historically primarily strike-slip kinematics experienced significant dip-slip motion (Berger et al., 2008; Pavlis et al., 2012; Schartman et al., 2019). The St. Elias region deformation front may also have shifted trenchward toward the south (Enkelmann et al., 2015a; Schartman et al., 2019).

The dynamic nature of the St. Elias syntaxis region has led to much debate on not only which faults are active and reactivated through time in this region but also the orientation kinematics of these structures (e.g., Bruhn et al., 2012). These concerns are compounded by some authors referring to the far-eastern contact fault as the Contact Fault (e.g., Bruhn et al., 2004), others referring to the far-eastern contact fault as the Bagley Fault (Bruhn et al., 2012), and still others having the Bagley Fault and Contact Fault being different structures (Berger et al., 2008; Chapman et al., 2012). Though beyond the spatial resolution of our results (estimated at ~10 km laterally at Moho depths; e.g., Lekić et al., 2011) to resolve these <5 km scale mapping concerns, we feel confident assuming that the Contact Fault and the BRF are not back thrusts because this would imply that these paleo-subduction interfaces have been overturned significantly.

12.3. DATA AND METHODS

The southern Alaska subduction zone has seen the deployment of multiple dense (<~20 km spacing) broadband seismometer arrays that cover most of the road system (Bauer et al., 2014; Daly et al., 2021; Ferris et al., 2003; Li et al., 2013; Tape et al., 2017). These dense arrays, supplemented with other permanent stations and smaller temporary arrays, provide excellent station density across the shallow subduction zone and allow for imaging of continuous features along-strike over hundreds of kilometers (e.g., Bauer et al., 2014; Kim et al., 2014). Recent P-to-S RF (Ps RF) imaging across southern Alaska (Mann et al., 2022) has revealed the continuity and subduction of the Yakutat oceanic plateau across the region, a thin low-velocity zone along the plate interface atop the subducting Yakutat crust, and a north–south-trending tear in the subducting slab below ~50 km depth (Brueseke et al., 2023). This newly imaged tear (Mann et al., 2022) has a broadly similar orientation but a different location than the tear inferred by Fuis et al. (2008).

In this study, teleseismic S waves recorded on seismometers across southern Alaska (Figure 12.1) were used to analyze the S-to-P scattered wavefield for crustal structure. Compared to Ps RFs, there are several advantages to using Sp RFs for regional seismic imaging. First, the conversion points are farther from the stations and can provide higher-fold imaging between stations that are spaced too far apart for overlapping Ps RF Fresnel zones at upper-plate depths. Second, Sp RFs contain one scattering mode (Figure 12.2), whereas Ps RFs record a superposition of multiple scattering modes resulting from surface-reflected and backscattered phases (e.g., Rondenay, 2009). Additionally, sedimentary basin multiples can obscure part of the record in Ps RFs (e.g., Cunningham & Lekić, 2019; Sheehan et al., 1995), but large basin multiples arrive after the S-wave arrival and therefore do not cause "ringing" in Sp RFs.

To generate the Sp CCP volume, S-wave data were analyzed following the procedure of Hua et al. (2020a). To improve vertical resolution of the Moho and other crustal velocity gradients, waveform data were filtered with a 2–30 s bandpass filter. We chose this filter to highlight crustal structure, in contrast to the Sp CCP stacking of Gama et al. (2022a), which employed a similar approach with a longer period bandpass (2–100 s) in order to optimize imaging of mantle structure. Particle motion analysis of the beginning of the P and S waves on the P and SV components, respectively, was conducted to estimate "surface" velocities at each station and was used with a free-surface transform (Kennett, 1991) to isolate the incident S wave from the converted P waves. All teleseismic S waves (Figure 12.1) recorded by the stations between 1 June 1999 and 19 April 2020 were analyzed, and events that had SV components with signal-to-noise ratio >1.5, defined as the ratio of the average within a 5 s signal window to that within a 25 s noise window, were used to generate Sp RFs. The resulting Sp RFs were migrated to their CCPs using a regional 3-D shear-velocity (V_s) model (Feng & Ritzwoller, 2019) and a 3-D compressive-wave velocity (V_p) model generated from that 3-D V_s model with shallow (<60 km) V_p/V_s constrained by RF phase stacking (Mann et al., 2022). The V_p/V_s for all points below the phase stacking depth were taken at each depth from the AK135 velocity model (e.g., Kennett et al., 1995). The Sp RFs were stacked on a 3-D grid of nodes (0.1° longitude × 0.1° latitude × 0.5 km in depth). At a given depth, the weighting of individual RFs at each point was determined with a horizontal Fresnel zone approximation based on 3-D Sp RF isochrons plus geometrical spreading and assuming nonzero weights only within the area where the "isochron slope angle" was less than 12° (see Hua et al., 2020a for full explanation).

Two other quality control parameters were used to cull the set of Sp RFs before stacking. First, Sp RFs that did not have a prominent negative-amplitude (associated with a PVG) Moho phase between 10 and 60 km depth were excluded (following Hua et al., 2020a). In Sp RFs, the most prominent phase is associated with the Moho, and even though the upper-plate Moho in subduction zones sometimes disappears or inverts in RF polarity (e.g., Bostock et al., 2002), we found that this step considerably improved the clarity of observed features in the CCP stack. Second, Sp RFs with anomalously high amplitudes in the mantle depth range were removed. Mantle velocity gradients are not expected to exceed those typically observed at the Moho (e.g., Krueger et al., 2021), so for times corresponding to the depth range of 100–450 km, Sp RFs with root-mean-square values greater than 0.2 were eliminated. These quality control steps resulted in 76,772 Sp RFs at the 734 stations, with an average of 105 per station. We use stations across a wider region of southern Alaska for our analysis, but we do not interpret results outside the regions of dense station spacing (Figures 12.1d and 12.2). Following Hua et al. (2020a), after stacking the Sp RFs at depth, interpretation of features was limited to the region with higher sampling, i.e., where the weighted stack value (Figure 12.1d; eq. 27 from Hua et al., 2020a) is greater than 0.4.

Resolution for RF signals depends on frequency content and velocity along the scattered-wave raypath (e.g., Rondenay, 2009). Assuming a minimum signal period of 2 s, Sp scattered-phase wavelengths at Moho depths should be 8–9.8 km (at the crust–mantle interface depths, V_s = 4.0–4.8 km/s), and vertical resolution for imaging subhorizontal discontinuities is therefore approximately 4–4.8 km, assuming that vertical resolution from

converted waves is approximately half a wavelength (Bostock, 1999).

Dip resolution for Sp CCP stacking is more difficult to quantify because it depends on a number of factors, including station spacing and distribution, the ray parameter and back-azimuthal ranges of incident S waves, signal-to-noise ratio, and the presence of adjacent boundaries. Overall, the shape of Sp RF sensitivity kernels yields better resolution of subhorizontal features (e.g., Hansen & Schmandt, 2017; Hua et al., 2020a, 2020b). However, tests with synthetic data show that shallow-dipping ($< \sim 15°$) intracrustal boundaries have been imaged using Sp CCP stacking along dense lines of stations (e.g., Hopper et al., 2017). At mantle depths, dip-resolution tests using CCP stacking of synthetics indicate that dipping boundaries are resolvable up to dips

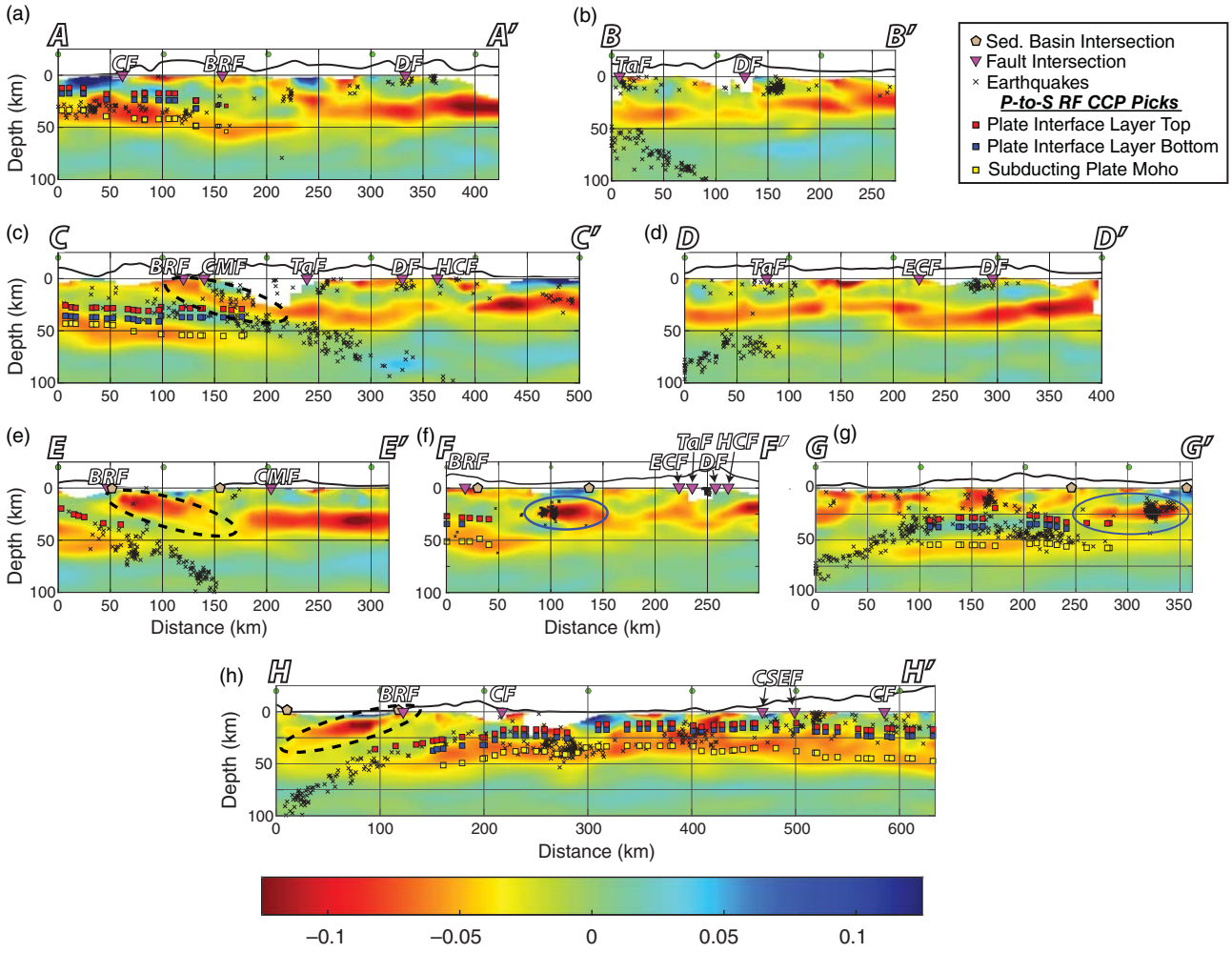

Figure 12.2 Cross sections through the Sp CCP volume analyzed in this study. Negative CCP stack amplitudes correspond to positive velocity gradients (PVGs), and positive stack amplitudes correspond to negative velocity gradients (NVGs). Each cross section is referenced as its own figure component, corresponding to the first letter of each line. For example, line A–A′ in panel (a). Small red, blue, and yellow squares plotted on each cross section are from Mann et al. (2022) Ps RF CCP imaging of the subducting Yakutat crust across the same region, using mostly the same seismometers. Small x symbols are earthquake hypocenters within 5 km of the cross section. Hypocenter locations are from Daly et al. (2021) to the east of 149°W (where they reported high-quality hypocenters) and from the Alaska Earthquake Center catalog to the west of 149°W. The locations where major faults (Figure 12.1b) cross each cross section are marked with an inverted magenta triangle. The locations where the lines cross the Copper River and Cook Inlet basins (Figure 12.1a) are in tan pentagons, plotted at $z = 0$ km. All fault labels (black and white lettering) are from Figure 12.1b. Blue ovals highlight the PVG discussed in the "Crustal Structure Beneath Copper River Basin Region" section. Black dashed ovals highlight PVG signal seen dipping inboard from the BRF. Green circles along cross sections denote locations along lines on the map in panel (i) on the following page.

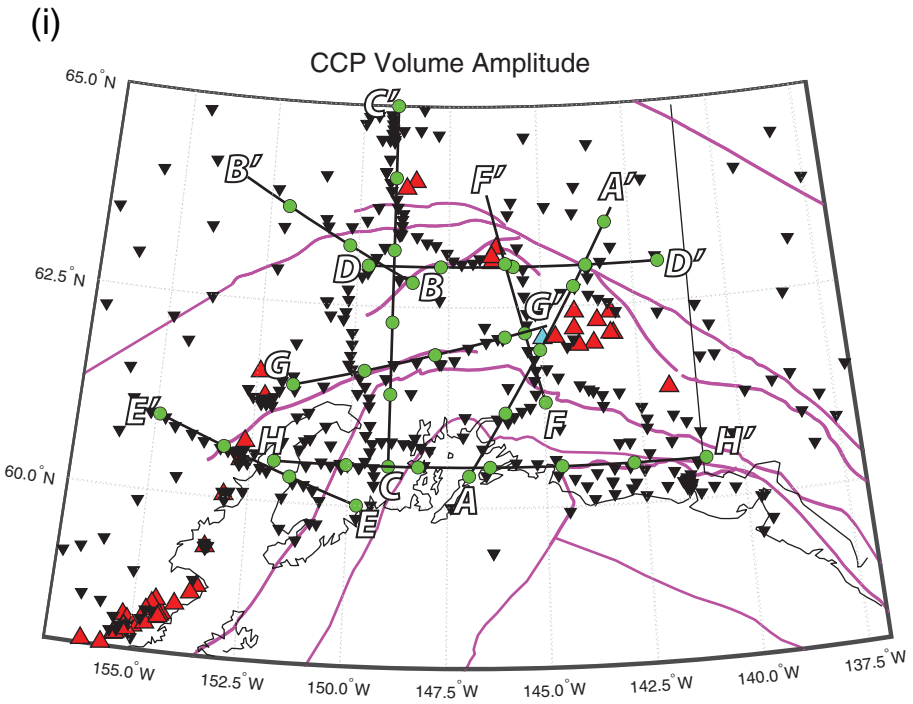

Figure 12.2 (*continued*)

of 10°–15° (Lekić & Fischer, 2017; Hua et al., 2020a). Even though this maximum resolvable dip (i.e., ~15°) may be an underestimate at crustal depths, we do not interpret features with apparent dips >~15°.

12.4. RESULTS

The Sp CCP volume contains clear features that represent conversions from the Moho and intracrustal interfaces. We categorize each velocity gradient interpreted here as a negative velocity gradient (NVG; velocity decreasing with depth) or PVG (velocity increasing with depth) instead of using RF polarity or CCP amplitude. PVGs correspond to negative Sp RF amplitudes (the convention used in the figures in this chapter), although in some other studies the sign of Sp amplitudes were flipped to match the association of PVGs with positive Ps amplitudes.

The most prominent feature in the Sp CCP volume is a consistent PVG in the upper 20–65 km depth range everywhere in the CCP volume. This PVG can be divided into two regions. In the south where subduction is occurring, the PVG strikes roughly parallel to the trench and dips inboard, and likely represents the Moho of the modern subducting slab. This interpretation is supported by the continuity of the PVG with the dipping seismicity associated with the subducting slab (Figure 12.2a,c,e,h). Across the remaining region, the PVG is subhorizontal between 20 and 50 km depth with some sharp offsets in depth and corresponds with the upper-plate Moho (Figure 12.2). In the southern subduction region, an NVG overlies and parallels the dipping PVG at depths <50 km nearly everywhere. This feature is likely the plate interface between subducting and overriding crust.

Other imaged features exist within the upper-plate crust across the region. At the western end, inboard-dipping PVGs extend from the surface to upper-plate Moho depths beneath the Kenai Peninsula and the region just to the north of the Kenai Peninsula (Figure 12.2c,e,h). These dipping PVGs intersect the surface at the trace of the BRF (Pavlis, 1982) but only exist along the western segment of the BRF system (west of ~149°W). Additionally, a strong subhorizontal PVG is imaged at ~25 km depth beneath the northern/northeastern portion of the Copper River Basin (Figure 12.2f,g). This PVG extends for over 100 km east–west (between 147°W and 145°W) and ~50 km north–south (between 62°N and 62.5°N). At this PVG's southeastern corner, the feature coincides with a dense cluster of earthquakes between 15 and 30 km depth (Figure 12.2f,g; Daly et al., 2021) directly beneath the Klawasi group mud volcanoes (Figure 12.1), which have mantle fluid isotopic signatures, are linked to an inferred deep-seated magmatic intrusive, and are located ~20 km to the west of the main Wrangell Volcanic Arc (Figure 12.1; Brueseke et al., 2019; Motyka et al., 1989).

12.5. DISCUSSION

12.5.1. The Subducting Yakutat Crust

The subducting Yakutat Moho is imaged nearly everywhere as an inboard-dipping PVG that agrees well with previous Ps RF imaging (Mann et al., 2022; Figure 12.2a,c,e,f). Along line G–G′, which is roughly along strike of the subducting Yakutat slab, the top and bottom of the western half of the Yakutat crust are imaged at ∼40 and ∼60 km depths, respectively. This provides further evidence that the Yakutat is subducting at a very shallow angle between 150°W and 147.5°W (Figure 12.2g), and this result matches the Ps RF imaging across the region quite well (e.g., Mann et al., 2022).

The plate interface is imaged as an NVG nearly everywhere atop the subducting Yakutat plateau in the Sp CCP imaging and parallels the Yakutat Moho (Figure 12.2). This NVG is colocated with a thin low-velocity layer (LVL) imaged atop the subducting Yakutat crust across the region using higher-resolution Ps RF phases (e.g., Kim et al., 2014; Mann et al., 2022). The Sp RF phases used here have slightly less volumetric resolution than the upgoing P-to-S analog conversion ("Pxs") and significantly less resolution than surface-reflected, backscattered RF phases. The fact that the plate interface appears as a single NVG here with lower Sp RF resolution (cf. Mann et al., 2022) suggests that the top boundary of the LVL generates a converted wave with greater amplitude than the bottom boundary of the LVL, and destructive interference between the two converted waves results in a single apparent NVG. The top of the LVL being a stronger velocity contrast is consistent with high-resolution local earthquake scattering analysis (e.g., Kim et al., 2019). Additionally, Ps RF migration images using only Pxs show an NVG across the top of the subducting crust where the higher-resolution surface-reflected RF phases show a thin low-velocity zone (e.g., Kim et al., 2014; Mann et al., 2022).

This single NVG along the plate interface resembles structures documented in subduction zones with thinner subducting crust (<10 km; e.g., Abers et al., 2009; Audet et al., 2009) than the Yakutat slab (11–30 km; Christeson et al., 2013; Ferris et al., 2003; Kim et al., 2014; Mann et al., 2022; Rondenay et al., 2008; Rossi et al., 2006; Worthington et al., 2012) and raises a long-debated question as to what this imaged feature represents. At these depths, the velocity of the overriding crust should be lower than in the subducting basalt, so an NVG at the interface between these two features is not expected without the presence of sediment and tectonically eroded material along the interface (e.g., Abers et al., 2009; Kim et al., 2014; Mann et al., 2022) or significant porosity and pore fluids (e.g., Peacock et al., 2011). Additionally, high-resolution seismic tomography models do not show a decrease in velocity across the interface, suggesting that the cause of the NVG is either too thin or too sparse to image completely (e.g., Calvert et al., 2020). Given the fact that Sp RFs have lower resolution than Ps RFs, and the subduction zone structure in this region has been extensively studied using Ps RFs (e.g., Kim et al., 2014; Mann et al., 2022), we only show the Ps RF CCP volume picks for the plate interface LVL and subducting Moho for comparison and to reinforce the crustal imaging results discussed below.

12.5.2. Upper-Plate Crustal Structure

We interpreted cross sections of the Sp CCP volume for crustal thickness and internal structure along paths that follow dense station spacing across the region. These cross sections are compared with the locations of other features, such as major faults, terrane boundaries, and earthquakes (Figure 12.2).

Border Ranges Fault

The BRF separates the inboard WCT from the seaward Chugach–Prince William Terrane (Pavlis, 1982) and is one of the most identifiable topographic surface features across Southern Alaska (Figure 12.3). The BRF began as a paleo-subduction zone plate interface that accommodated northward subduction beneath the WCT from Early Jurassic to Late Cretaceous time (e.g., Pavlis & Roeske, 2007; Trop & Ridgway, 2007). Only scattered remnants of this paleo-subduction interface are still identifiable at the surface. The BRF system now consists of several branches that have juxtaposed different rock packages at different times (Plafker et al., 1989).

An inboard-dipping PVG extends from the surface trace of the BRF to >25 km depths across the northern and western sides of the Kenai Peninsula (Figure 12.2c,e,h). The north–south line C–C′ shows this feature dipping to the north at ∼15° extending from the BRF at the surface to the continental Moho (Figure 12.2c). Along lines E–E′ and H–H′, a similar feature dips to the west at ∼15° beneath the Cook Inlet Basin (Figure 12.2e,h). We considered three geologic features that may be related to this PVG. (1) The PVG may be the top of accreted, high-velocity ultramafic–mafic rocks of the Border Ranges ultramafic and mafic assemblages that lie along the BRF system (e.g., Clark, 1973; Kusky et al., 2007; Plafker et al., 1989). (2) The PVG may be a sliver of Border Ranges ultramafic and mafic assemblages at shallow depths followed by the top of a subhorizontal serpentinized body in the lower crust seen at ∼15 km depth beneath the southeastern part of Cook Inlet Basin (Mankhemthong et al., 2013). (3) The PVG is a signal

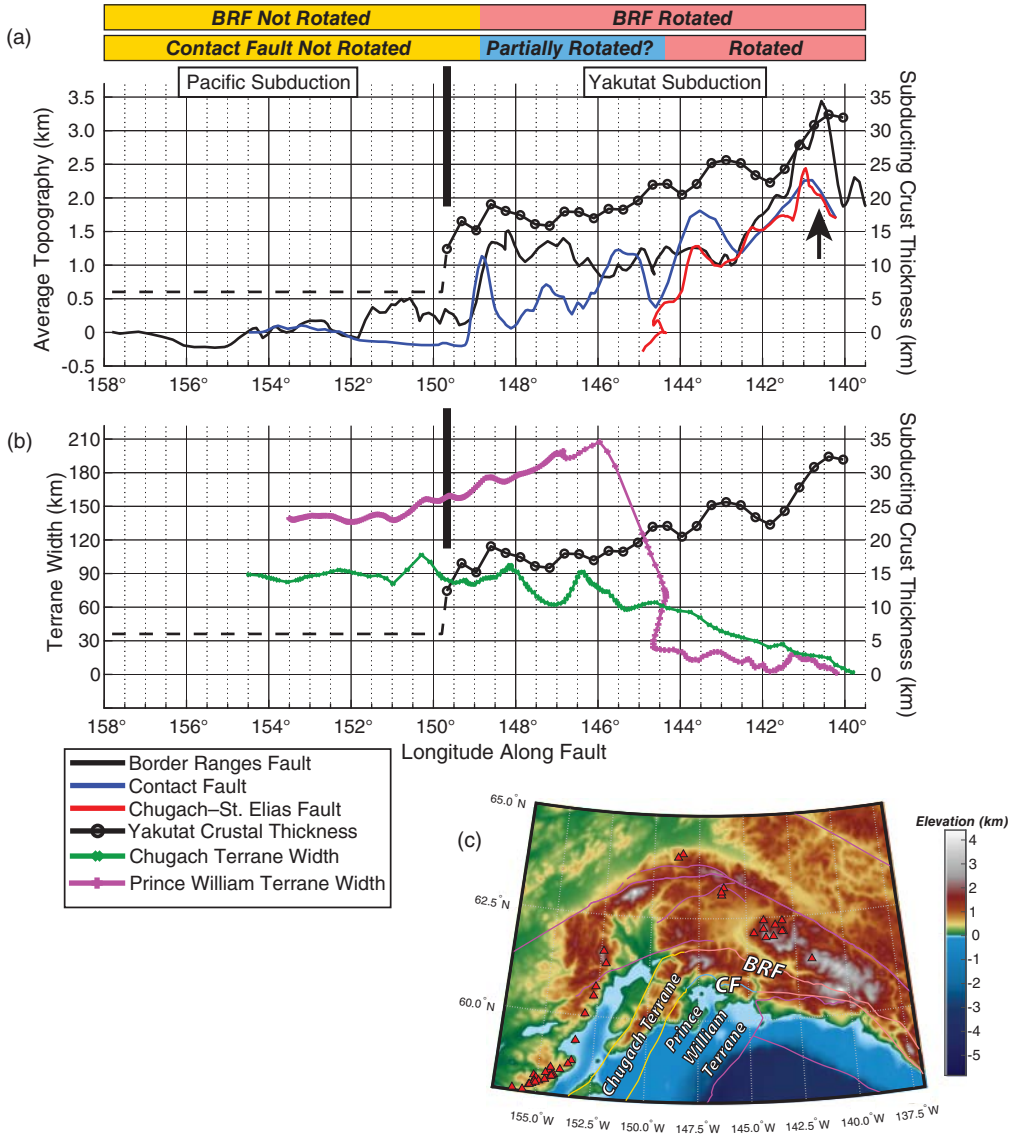

Figure 12.3 Analysis of topography along the BRF and Contact Fault, and the intervening terranes' approximate thicknesses. It is inferred that the BRF is rotated to subvertical to the east of ~149°W, whereas the Contact Fault is rotated to subvertical to the east of ~145°W. (a) Comparison of subducting Yakutat thickness from Mann et al. (2022) with average topography within 5 km of each fault trace, plotted at the longitude of the fault. The arrow highlights the location of St. Elias syntaxis and collision (Chapman et al., 2012; Enkelmann et al., 2010, 2015a, 2015b) of the thickest Yakutat Terrane (Brueseke et al., 2023; Mann et al., 2022; Worthington et al., 2012). (b) Comparison of subducting Yakutat thickness with approximate widths of the Prince William and Chugach Terranes. (c) The peach color indicates portions of the Border Ranges and Contact faults that have been rotated to subvertical. Unrotated sections are denoted by yellow lines. Potentially partially rotated section of Contact Fault is denoted by blue line. These are also shown at top of the figure plotted versus longitude. Shades of magenta coloring show offshore Yakutat crustal thickness variations (Worthington et al., 2012).

from the base of the ~5–7-km-thick Cook Inlet Basin (Shellenbaum et al., 2010).

If the inboard-dipping PVG is the top of a serpentinized body, then the serpentinization could have resulted from fluid interaction within the overriding crust when the BRF was the subduction interface. However, serpentinization decreases seismic velocities (e.g., Bostock et al., 2002), so RF phases with the opposite polarity (i.e., NVG) may be expected, depending on the degree of serpentinization (Hyndman & Peacock, 2003). While the inboard-dipping PVG does not preclude serpentinization of the lowermost crust below the Kenai Peninsula and Cook Inlet Basin

(e.g., Mankhemthong et al., 2013), it is unlikely that such a strong PVG could result from the top of a serpentinized body at these shallow crustal depths.

If the PVG is the base of the overlying Cook Inlet Basin, then this PVG is simply an imaging artifact. However, the geometry of the PVG is inconsistent with this interpretation. Sp RF phases are expected from the base of the overlying Cook Inlet Basin, but such arrivals would likely be subhorizontal across much of the basin (Kim et al., 2014; Shellenbaum et al., 2010; Smith & Tape, 2020). For example, the base of the ~5–7-km-thick Cook Inlet Basin (Shellenbaum et al., 2010) should create a subhorizontal PVG from $x = 0$ to 120 km on line H–H′. However, the apparently subhorizontal part of the PVG only exists in the southeastern end of the basin, even though a subhorizontal PVG segment is expected throughout the basin given that there is more than sufficient station coverage (Figure 12.2e,h). The inboard-dipping PVG seems to continue beneath the basin to depths >25 km. Moreover, the PVG is seen both outside the boundary of Cook Inlet Basin (line C–C′) and within the basin (lines E–E′ and H–H′). Therefore, we do not think that the dipping PVG is the result of artifacts from basin conversions.

We prefer the interpretation that the PVG feature is related to the inboard-dipping Mesozoic paleo-subduction interface along the BRF system between the inboard WCT and Border Range ultramafic and mafic assemblages (Clark, 1973; Kusky et al., 2007; Pavlis et al., 2019), with the Cook Inlet Basin conversions superimposed over this PVG feature in the Sp CCP volume along lines E–E′ and H–H′. The next seaward terrane boundary, the Contact Fault (Figure 12.1b), has shallow, inboard-dipping structures beneath it as well (e.g., Eberhart-Phillips et al., 2006; Fisher et al., 1983; Stephens et al., 1990; Ye et al., 1997) although they are too shallow and/or small scale to image with the Sp data in this study.

Both the BRF and Contact Fault were reactivated and experienced strike-slip motion during the Paleocene–Eocene (Berger et al., 2008; Bol & Roeske, 1993; Pavlis & Roeske, 2007). It has been documented that paleo-subduction interfaces can experience strike-slip motion without reorganization or rotation toward vertical of deep structure (e.g., Sato et al., 2015). However, the preservation of low-angle dip of the BRF paleo-subduction interface along the western segment (i.e., Kenai Peninsula) may in part explain why major strike-slip Eocene displacement (Garver & Davidson, 2015) was transferred onto other structures (Pavlis & Roeske, 2007). Strike slip along the western BRF region may have been accommodated on the nearby Eagle River Fault (Pavlis & Roeske, 2007; Amato et al., 2013; Malik, 2019) and/or the Castle Mountain Fault (Pavlis & Roeske, 2007).

There are no apparent shallow-dipping features in this CCP volume to the east of ~149°W, where the buoyant Yakutat oceanic plateau has been subducting since ca. 30 Ma (e.g., Brueseke et al., 2019). This could mean that the dip of the BRF has been rotated toward vertical through extensive contraction and is now dipping too steeply to image with Sp CCP stacking (e.g., Arkle et al., 2013; Enkelmann et al., 2010; Mankhemthong et al., 2013).

The BRF east of ~149°W may have been rotated toward vertical during the oblique transport and accretion of the Chugach and Prince William Terranes. Conversely, if contraction related to buoyant Yakutat subduction is in part the reason for the absence of the imaged BRF paleo-subduction interface, the Contact Fault paleo-subduction interface managed to be preserved at least to 145.2°W with an inboard dip of ~30° under the central segment (Figure 12.3), as seen in active-source seismic studies (e.g., Fuis et al., 1991). The lithological similarities of the Chugach and Prince William Terranes (deep-water turbidites both sides of the Contact Fault) may in part explain why west of 145.2°W the Contact Fault was not rotated compared to the BRF (deep-water turbidites to the south and oceanic plateau–island arc to the north), which has a greater across-strike change in crustal properties (Mankhemthong et al., 2013; Trop & Ridgway, 2007).

To further investigate the relationships between upper-plate deformation and the inferred along-strike variation in dips of the BRF and Contact Faults, we measured along-strike variations in topography by averaging values within 5 km of each terrane-bounding fault near the subduction zone (i.e., BRF, Contact Fault, and Chugach–St. Elias Fault) and also estimated the strike-normal thickness of both the Chugach and Prince William Terranes (Figure 12.1b). These values were compared with subducting Yakutat crustal thickness beneath the margin (from Mann et al., 2022; Figure 12.3). A sharp change in topography along the major faults at ~149°W corresponds with the point between Yakutat subduction to the east and Pacific Plate subduction to the west (Kim et al., 2014; Mann et al., 2022). Additionally, the width of both the Chugach and Prince William Terranes decreases to the east, with the Prince William Terrane eventually pinching off around the collisional zone at ~141°W (e.g., Chapman et al., 2012) where the subducting Yakutat crustal thickness exceeds 25–30 km (Figure 12.3). The elevation and terrane width trends indicate significant shortening and deformation across the eastern half of the region, probably related to buoyant Yakutat crust subduction (e.g., Abers, 2008). The west to east transition from low to high deformation at ~149°W is well correlated with the rotation of the BRF to a steeper dip inferred from Sp CCP stacking and previous studies (Arkle et al., 2013;

Enkelmann et al., 2010; Mankhemthong et al., 2013). As previously described, the similar rotation toward vertical inferred for the Contact Fault (e.g., Fuis et al., 1991) occurs farther east, perhaps indicating that the western limit of the most intense deformation in the more seaward terranes is also offset to the east. This latter conclusion is broadly consistent with the along-strike topographic gradients for the Contact and Chugach–St. Elias faults (Figure 12.3).

Where the Pacific Plate is subducting to the west of the imaged Yakutat plateau (Kim et al., 2014; Mann et al., 2022; Rondenay et al., 2008; Worthington et al., 2012) (i.e., west of ~149°W), the long-term exhumation rate is ~0.1 mm/year (Valentino et al., 2016), and there has been a minimum of exhumation (<2–3 km) and inferred shortening since ca. 30 Ma. Arkle et al. (2013) demonstrated, with applied thermochronology, that the Contact Fault is a structural barrier along the central segment (Figure 12.1), with >11 km of Oligocene-to-Present exhumation north of the fault (exhumation rate of ~0.7 mm/year) and just a few kilometers of exhumation (exhumation rate of ~0.2 mm/year) to the south during the same time frame. Hence, the Contact Fault paleo-subduction interface may have played a role in focusing Oligocene-to-Present deformation to the north in this region. Furthermore, in the central segment the BRF paleo-subduction interface was rotated to a subvertical position and also facilitated vertical tectonics (Figure 12.4). In this scenario, the Maastrichtian(?)-to-Paleogene Contact Fault paleo-subduction interface (Bol & Roeske, 1993; Brocher et al., 1994; Davidson & Garver, 2017; Fuis & Plafker, 1991) would be reactivated during the Oligocene–Neogene Yakutat shallow subduction event (e.g., Arkle et al., 2013).

There is no seismic imaging of the geometry of the Contact Fault east of 145.2°W, but it has been inferred that the fault was rotated toward vertical after ca. 5 Ma (Chapman et al., 2012; Enkelmann et al., 2008). In this region, where both the BRF and Contact Fault have inferred subvertical dips, exhumation rates in places are >5 mm/year (Enkelmann et al., 2015b). The west to east variability in BRF and Contact Fault structural geometry aligns with known exhumation patterns (Arkle et al., 2013; Enkelmann et al., 2015b; Valentino et al., 2016). Low-angle structures are inefficient at exhumation and accommodate contraction more through horizontal than vertical motion (e.g., Reiners & Brandon, 2006), whereas vertical structures facilitate vertical extrusion of crustal blocks (e.g., Benowitz et al., 2022). Overall, the dramatic

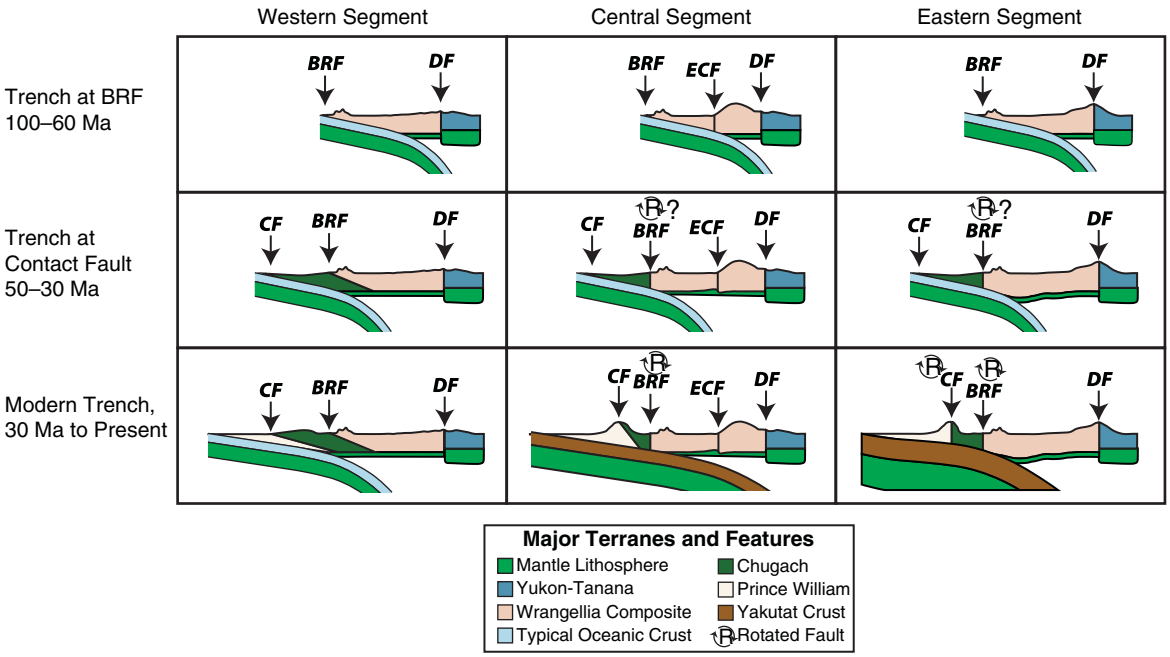

Figure 12.4 Schematic depicting snapshots through time of each of the three segments (Figure 12.1c) and whether or not the BRF and/or Contact Fault have been rotated toward subvertical. The central and eastern segments of BRF may have been rotated during ca. 60–50 Ma oblique translation and accretion of the Chugach and Prince William Terranes or this fault rotation from ~15° toward subvertical may be related, at least in part, to the Yakutat oceanic plateau subduction. Only the eastern segment of the Contact Fault has been rotated from ~15° to ~30° toward subvertical where the Yakutat slab is the thickest (Figure 12.3). See the text for further discussion and references. Note: thicknesses and dip angles in this figure are not drawn to scale.

along-strike variability in structural dip of the BRF and Contact Fault implies three different structural configurations operating along the same Oligocene-to-Present trench, aligning with previous work that has highlighted margin-parallel variations in deformation history (Figure 12.4; Arkle et al., 2013; Buscher et al., 2008; Enkelmann et al., 2010; Valentino et al., 2016).

Denali and Hines Creek Faults

The upper-plate Moho typically shallows by 5–10 km northward across the Denali Fault system in the profiles analyzed in this study (Figure 12.2a–c,f). The one exception is line D–D′, where a shallowing of the Moho across the Denali Fault is more gradual. Crustal thickness of the Yukon-Tanana Terrane, which is north of the Denali Fault, is only analyzed along lines of dense station spacing to avoid artifacts due to sparse sampling of the CCP volume. The Moho offset across the Denali Fault system has been imaged by fault-zone head-wave analysis (Allam et al., 2017), RF migration (Allam et al., 2017; Mann et al., 2022; Miller et al., 2018), inversions of surface-wave data (Haney et al., 2020), joint inversion of RFs and surface-wave data (e.g., Gama et al., 2022b; Martin-Short et al., 2018), and other imaging techniques (for a review; see Yang et al., this volume). In the Hines Creek Fault region (Figure 12.1b), prior studies have found that the crustal thickness step is larger across the Hines Creek Fault than the Denali Fault (e.g., Allam et al., 2017; Miller et al., 2018; Rossi et al., 2006; Veenstra et al., 2006). On the comparable profile from the Sp CCP stack in the study (line C–C′; Figure 12.2c) the apparent Moho offset actually lies somewhat closer to the Denali Fault than to the Hines Creek Fault, which at this longitude lies ~20 km to the north. However, this difference may reflect the lower horizontal resolution provided by Sp phases, relative to Ps data at a comparable period (e.g., Hansen & Schmandt, 2017; Hua et al., 2020a, 2020b; Mancinelli & Fischer, 2017).

Eureka Creek Fault

The most prominent Moho depth offset imaged across the region in the Sp CCP volume is a ~15 km eastward increase in crustal thickness on line D–D′ (Figure 12.2d) where it crosses the mapped surface trace of the Eureka Creek Fault (Nokleberg et al., 1985). There is also an ~10 km northward increase in crustal thickness across the Eureka Creek Fault along line D–D′. These crustal thickness offsets are very close to the location of newly discovered volcanoes and fissures that lie above the western limb of the tear in the subducting Yakutat slab (Figure 12.1a; Brueseke et al., 2023).

The Eureka Creek Fault juxtaposes two significantly different subterranes of the WCT: the Tangle subterrane to the south and the Slana River subterrane to the north (Nokleberg et al., 1985). Not much had been known about the orientation of the Eureka Creek Fault at depth nor its slip history (e.g., Nokleberg et al., 1985, 1989), but the apparent vertical offset in Moho thickness across the fault is likely an inherited feature from when these two subterranes were juxtaposed across an active strike-slip fault. Overall, the Eureka Creek Fault represents a good example of an ancient subterrane-bounding fault maintaining crustal thickness offsets through time.

Crustal Structure Beneath Copper River Basin Region

The PVG imaged at ~25 km depth beneath the Copper River Basin extends approximately from 147°W to 145°W, and 62°N to 62.5°N (Figure 12.2f,g). The maximum thickness of the basin reaches ~2 km (Fuis et al., 1991; Powell & Amoco Oil Co, 2019), which would result in PVGs at depths <10 km, so this feature is not related to conversions at the base of the basin. However, the PVG does extend throughout the basin and may indicate a link between these features.

The mid-crustal PVG is directly above the ca. 1 Ma shallow tear in the subducting Yakutat slab (Figure 12.5; Brueseke et al., 2023; Mann et al., 2022). A dense cluster of earthquake hypocenters falls at the southeastern boundary of the PVG, near the Klawasi group mud volcanoes (Figure 12.5; Daly et al., 2021). An NVG follows the

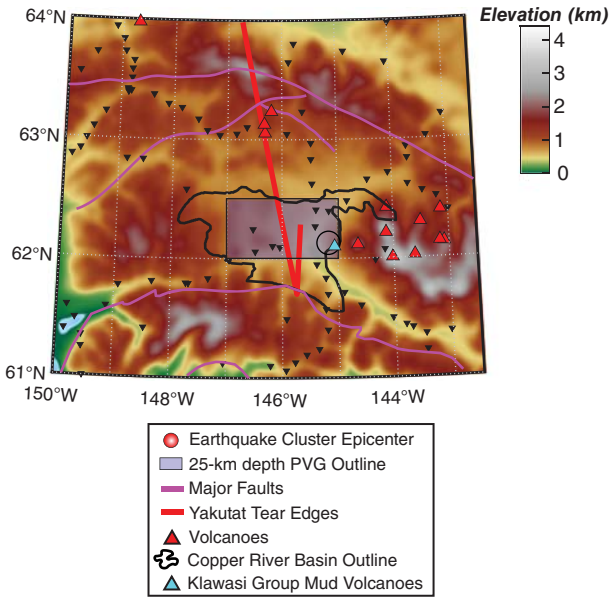

Figure 12.5 Zoom-in of the Copper River Basin and subducting Yakutat slab tear region (outline shown in Figure 12.1a), highlighting the coincidence of (1) the earthquake cluster at ~25 km depth immediately to the west of the Wrangell Arc (Daly et al., 2021), (2) the PVG seen at ~25 km depth beneath the Copper River Basin, and (3) underlying subducting slab tear location (Mann et al., 2022).

PVG at 25 km depth in the southeastern corner, which is especially pronounced beneath the cluster of earthquakes (Figure 12.2g), and finally beneath that is a weak PVG at ∼50 km depth which matches the depth where there is a velocity increase in both Ps RF imaging (Mann et al., 2022) and along the Trans-Alaska Crustal Transect (TACT) lines (e.g., Fuis et al., 1991).

Other studies have also found anomalous structures beneath the Copper River Basin. The north–south TACT line through the eastern part of the basin reported compressional velocities of ∼6.7–6.9 km/s (e.g., Fuis & Plafker, 1991) below ∼20 km depth which more closely match that of basalt and not continental crust (Brocher, 2005). Refracted P waves from explosions in College Fjord at the northwest corner of Prince William Sound were recorded traveling at ∼6.8 km/s at stations along the Richardson Highway (paralleling line F–F′, Figure 12.2f) but arrived ∼1 s delayed along paths crossing this region (Hales & Asada, 1966). This delay was interpreted as resulting from anomalous lower crust and uppermost mantle velocities along these paths and is not the result of Moho depth variations. Additionally, the TACT line extending east–west through the Copper River Basin recorded no Pn or PmP throughout this region, further suggesting that the lower crust and uppermost mantle beneath this region are anomalous (Goodwin et al., 1989).

Based on the TACT active-source experiment results, the region from 20 to 50 km depth beneath the Copper River Basin was interpreted as having formed from three possible scenarios: (1) north-to-south tectonic underplating of lower North American crust beneath the Wrangellia and Peninsular Terranes, (2) south-to-north tectonic underplating by the Kula Plate, or (3) magmatic underplating at some point since the late Cretaceous (Fuis & Plafker, 1991). Tectonic underplating of lower North American crust from the north is not supported by the presence of the sharp offset in crustal thickness across the Eureka Creek Fault just to the north of this region (see the Eureka Creek Fault section). Such a crustal thickness offset probably would have been obliterated if buoyant lower crust was underthrust southward beneath the region. The subvertical lithospheric-scale nature of the Denali–Hines Creek fault (Gama et al., 2022b; Newell et al., 2023) further discounts scenario (1). Furthermore, the imaged inboard-dipping BRF Mesozoic paleo-subduction interface supports a model of inboard-dipping (east and northward) subduction polarity from the Mesozoic to the Present (Pavlis et al., 2019).

Between the two remaining possible scenarios, (2) and (3), we prefer the interpretation that the source of the subhorizontal mid-crustal PVG is due to magmatic underplating and/or intrusion. The location of this feature abutting against the western limb of the torn Yakutat slab and directly above a nascent slab window (Figure 12.5; Brueseke et al., 2023; Mann et al., 2022), next to the WVF and below Holocene mud volcanoes, and overlapping with a dense cluster of earthquakes (Daly et al., 2021) suggests a connection between subducting slab tearing, crustal structure, and volcano formation.

This scenario raises interesting questions about crustal thickness across the region. If the sharp PVG at ∼25 km depth beneath the Copper River Basin is the base of the Moho, then ponding of basaltic melt into the thin (Gama et al., 2022a) mantle lithosphere of the upper plate may explain the weak underlying PVG at ∼50 km depth and the velocities seen in the TACT experiment (Fuis et al., 1991). This scenario would imply that there is a ∼20–25-km-thick layer of mantle containing ponded melt beneath the upper plate, directly above the tear in the subducting slab. However, if the PVG at ∼50 km depth (Figure 12.2g; Fuis et al., 1991; Ward & Lin, 2018) is the upper-plate Moho, then this would require a very large 20–25 km eastward increase in Moho depth within the Copper River Basin to accommodate the shallow Yakutat slab imaged at ∼30 km depth on its western end (Figure 12.2). Maintaining such an abrupt crustal thickness offset over a geologically significant amount of time would be especially challenging in the dynamically active environment created by the subduction of Yakutat crust. Therefore, we prefer the interpretation that the PVG at ∼25 km depth is the upper-plate Moho beneath the Tangle subterrane of the WCT (e.g., Nokleberg et al., 1985). This scenario would mean that the reduced velocities in the mantle lithosphere and underlying mantle (i.e., between ∼20 and 50 km depth) seen in active-source results (Fuis et al., 1991), local explosion traveltime analysis (e.g., Goodwin et al., 1989; Hales & Asada, 1966), and recent tomographic results from a joint inversion of RFs and surface wave data (e.g., Ward & Lin, 2018) suggest significant underplating and intrusion of basaltic magmatism into the upper plate, rising from the shallow tear in the subducting Yakutat slab.

All of these features point toward significant alteration of the crust immediately to the west of the Wrangell Volcanic Field and east of the shallow-dipping subducting Yakutat slab (Figure 12.5), directly above the tear in the subducting Yakutat slab. A tear or window in a subducting slab would allow for influx of hot asthenospheric mantle into the mantle wedge (e.g., Jadamec, 2016; Jadamec & Billen, 2012; Király et al., 2020) and may rapidly dehydrate and eclogitize subducting crust, leading to significant alterations in the tectonics of the subducting Yakutat slab (e.g., Brueseke et al., 2023), increase in mantle flow (e.g., Jadamec & Billen, 2010), and partial melting rising to the surface which may pond beneath and/or intrude the upper-plate crust. Given the

cessation of the westward/northwestward younging age trend and magmatism of the Wrangell Arc at ca. 1 Ma (Richter et al., 1990; Trop et al., 2022), we speculate that the coincidence of the various geophysical observations directly beneath the Klawasi group mud volcanoes just to the west of the youngest Wrangell Arc volcanos (e.g., Sanford, Drum, Wrangell; Figure 12.5; Trop et al., 2022) is evidence that these mud volcanos may be signs of growth of the next-generation Wrangell Volcanic Field tear volcano.

12.6. CONCLUSIONS

The relatively high-resolution Sp CCP imaging presented here provides one of the best images of crustal architecture across the active Alaskan convergent margin that is free from the effects of reverberations found in Ps RF studies and that samples more widely than active-source studies. This kind of imaging is only possible due to decades of work deploying dense seismometer arrays across the region, which allow for imaging and tracing of upper-plate crustal architecture across the region.

Major findings include the following:

1. The plate interface is imaged as an NVG above the parallel subducting slab Moho across the Yakutat slab shallow subduction region and agrees well with previous Ps RF imaging.
2. This southern Alaska Sp CCP imaging, combined with previous seismic imaging (e.g., Fuis et al., 1991; Stephens et al., 1990; Ye et al., 1997), and tectonic reconstructions (e.g., Trop & Ridgway, 2007) provide insight into why low-angle paleo-subduction interfaces are preserved in some locations and rotated toward vertical with time in other places along the margin. The western segment of the BRF preserves the inboard (paleo-east) dipping (~15°) Mesozoic paleo-subduction interface to at least ~25 km depth, but there the BRF may extend further to the upper-plate Moho at ~35 km depth. The next seaward terrane boundary, the Contact Fault between the Chugach Terrane and the Prince William Sound Terrane, is also imaged along the western segment as a shallow-dipping (~15°) detachment (e.g., Stephens et al., 1990; Ye et al., 1997). In the central transitional segment, the BRF subduction interface is rotated toward vertical (Figure 12.2; e.g., Fuis et al., 1991), but the Contact Fault is not (dips ~30°; Fuis et al., 1991), whereas both the BRF and Contact Fault are rotated toward vertical along the eastern segment (Figure 12.3; Chapman et al., 2012; Enkelmann et al., 2008). These seismic observations in part reflect the differences in Oligocene-to-Present slab thickness between the Pacific and Yakutat segments of the BRF and across-fault lithologic variations. To the east, both the BRF and Contact Fault have been rotated toward vertical where the Yakutat plateau crust is thickest (~25 to 30 km), and this contraction is evidenced by significant shorting across the Prince William Terrane (Figure 12.3). In summary, Eocene soft-docking of the Chugach and Prince William Terranes via strike-slip faulting (Garver & Davidson, 2015) limited Oligocene-to-Present contraction, and ongoing Pacific slab subduction along the western segment (Buscher et al., 2008; Valentino et al., 2016) has preserved the Mesozoic BRF and the Eocene–Oligocene Contact Fault subduction interface.
3. Discrete upper-plate Moho offsets across terrane (Denali-Hines Creek faults) and sub-terrane (Eureka Creek Fault) boundaries on the order of 10 km highlight significant Mesozoic crustal-scale terrane tectonics. The imaged inboard-dipping BRF Mesozoic paleo-subduction interface supports a model of inboard-dipping (east and northward) subduction polarity from the Mesozoic to the Present (Pavlis et al., 2019), which is also consistent with the upper-plate Moho offsets.
4. We conclude that the newly imaged crust beneath the Copper River Basin, which likely has a thickness of ~25 km, is underplated and significantly magmatically intruded and altered, potentially due to excessive melt rising from the underlying slab tear and ponding beneath the upper-plate crust (Daly et al., 2021; Mann et al., 2022). These features and the overlying mud volcanos with mantle fluid isotopic signatures (Motyka et al., 1989) indicate potential for the creation of a new Yakutat slab tear volcano in the Wrangell Volcanic Field.

In summary, by applying Sp RF imaging along dense lines of seismometers, we document the preservation of Jura-Cretaceous terrane boundaries and a Mesozoic paleo-subduction interface and the along-strike rotation toward vertical of the same paleo-subduction interface due at least in part to Oligocene-to-Present buoyant Yakutat oceanic plateau subduction. Along-strike variations in subduction zone indenter history and across-strike lithological contrasts are common features of many long-lived convergent margins, and the results of this study may have bearing on how inherited crustal features affect later deformation patterns globally.

ACKNOWLEDGMENTS

We thank J. Hua for help in implementing the CCP stacking codes. The manuscript was improved through the comments and suggestions of S. Gulick, G. Fuis, and two anonymous reviewers and benefitted from the foundational work of the USGS Trans-Alaska Crustal Transect

(TACT) project. This work was supported by NSF EAR-2053042 and Woods Hole Oceanographic Institution OBS Instrument Center Postdoctoral Scholarship (M.E.M.) and NSF EAR-1829401 (K.M.F.).

AVAILABILITY STATEMENT

All data used in this study were obtained from the IRIS Data Management Center (https://ds.iris.edu/ds/nodes/dmc). IRIS Data Services are funded through the Seismological Facilities for the Advancement of Geoscience and EarthScope (SAGE) Proposal of the National Science Foundation (NSF) under Cooperative Agreement EAR-1261681.

REFERENCES

Abers, G. A. (2008). Orogenesis from subducting thick crust and evidence from Alaska. In J. T. Freymueller, et al. (Eds.), *Active tectonics and seismic potential of Alaska, geophysical monograph series* (Vol. *179*, pp. 337–349). AGU. http://dx.doi.org/10.1029/179GM19

Abers, G. A., MacKenzie, L. S., Rondenay, S., Zhang, Z., Wech, A. G., & Creager, K. C. (2009). Imaging the source region of Cascadia tremor and intermediate-depth earthquakes. *Geology*, *37*(12), 1119–1122. http://dx.doi.org/10.1130/G30143A.1

Allam, A. A., Schulte-Pelkum, V., Ben-Zion, Y., Tape, C., Ruppert, N., & Ross, Z. E. (2017). Ten kilometer vertical Moho offset and shallow velocity contrast along the Denali fault zone from double-difference tomography, receiver functions, and fault zone head waves. *Tectonophysics*, *721*, 56–69. http://dx.doi.org/10.1016/j.tecto.2017.09.003

Amand, P. S. (1957). Geological and geophysical synthesis of the tectonics of portions of British Columbia, the Yukon territory, and Alaska. *Geological Society of America Bulletin*, *68*(10), 1343–1370.

Amato, J. M., Pavlis, T. L., Clift, P. D., Kochelek, E. J., Hecker, J. P., Worthman, C. M., & Day, E. M. (2013). Architecture of the Chugach accretionary complex as revealed by detrital zircon ages and lithologic variations: Evidence for Mesozoic subduction erosion in south-central Alaska. *Bulletin*, *125*(11–12), 1891–1911.

Arkle, J. C., Armstrong, P. A., Haeussler, P. J., Prior, M. G., Hartman, S., Sendziak, K. L., & Brush, J. A. (2013). Focused exhumation in the syntaxis of the western Chugach Mountains and Prince William Sound, Alaska. *Bulletin*, *125*(5–6), 776–793.

Audet, P., Bostock, M. G., Christensen, N. I., & Peacock, S. M. (2009). Seismic evidence for overpressured subducted oceanic crust and megathrust fault sealing. *Nature*, *457*(7225), 76–78. http://dx.doi.org/10.1038/nature07650

Bauer, M. A., Pavlis, G. L., & Landes, M. (2014). Subduction geometry of the Yakutat terrane, southeastern Alaska. *Geosphere*, *10*(6), 1161–1176. http://dx.doi.org/10.1130/GES00852.1

Benowitz, J. A., Davis, K., & Roeske, S. (2019). A river runs through it both ways across time: $^{40}Ar/^{39}Ar$ detrital and bedrock muscovite geochronology constraints on the Neogene paleodrainage history of the Nenana River system, Alaska Range. *Geosphere*, *15*(3), 682–701.

Benowitz, J. A., Roeske, S. M., Regan, S. P., Waldien, T. S., Elliott, J. L., & O'Sullivan, P. B. (2022). Large-scale, crustal-block vertical extrusion between the Hines Creek and Denali faults coeval with slip localization on the Denali fault since ca. 45 Ma, Hayes Range, Alaska, USA. *Geosphere*, *18*(3), 1030–1054.

Berger, A. L., Spotila, J. A., Chapman, J. B., Pavlis, T. L., Enkelmann, E., Ruppert, N. A., & Buscher, J. T. (2008). Architecture, kinematics, and exhumation of a convergent orogenic wedge: A thermochronological investigation of tectonic–climatic interactions within the central St. Elias orogen, Alaska. *Earth and Planetary Science Letters*, *270*(1–2), 13–24.

Bol, A. J., & Roeske, S. M. (1993). Strike-slip faulting and block rotation along the contact fault system, eastern Prince William Sound, Alaska. *Tectonics*, *12*(1), 49–62.

Bostock, M. G. (1999). Seismic waves converted from velocity gradient anomalies in the Earth's upper mantle. *Geophysical Journal International*, *138*(3), 747–756. https://doi.org/10.1046/j.1365-246x.1999.00902.x

Bostock, M. G., Hyndman, R. D., Rondenay, S., & Peacock, S. M. (2002). An inverted continental Moho and serpentinization of the forearc mantle. *Nature*, *417*(6888), 536–538. http://dx.doi.org/10.1038/417536a

Brennan, P., Gilbert, H., & Ridgway, K. D. (2011). Crustal structure across the Central Alaska range: Anatomy of a Mesozoic collisional zone. *Geochemistry Geophysics Geosystems*, *12*(4).

Brocher, T. M. (2005). Empirical relations between elastic wavespeeds, & density in the Earth's crust. *Bulletin of the Seismological Society of America*, *95*(6), 2081–2092. http://dx.doi.org/10.1785/0120050077

Brocher, T. M., Fuis, G. S., Fisher, M. A., Plafker, G., Moses, M. J., Taber, J. J., & Christensen, N. I. (1994). Mapping the megathrust beneath the northern Gulf of Alaska using wide-angle seismic data. *Journal of Geophysical Research: Solid Earth*, *99*(B6), 11663–11685.

Brueseke, M. E., Benowitz, J. A., Bearden, A. T., Mann, M. E., & Miggins, D. P. (2023). Subduction disruption, slab tears: ca. 1 Ma true collision of an ~30-km-thick oceanic plateau segment recorded by Yakutat slab nascent tear magmatism. *Terra Nova*, *35*, 49–57. http://dx.doi.org/10.1111/ter.12628

Brueseke, M. E., Benowitz, J. A., Trop, J. M., Davis, K. N., Berkelhammer, S. E., Layer, P. W., & Morter, B. K. (2019). The Alaska Wrangell Arc: ~30 Ma of subduction-related magmatism along a still active arc-transform junction. *Terra Nova*, *31*(1), 59–66.

Bruhn, R. L., Pavlis, T. L., Plafker, G., & Serpa, L. (2004). Deformation during terrane accretion in the Saint Elias orogen, Alaska. *Geological Society of America Bulletin*, *116*(7–8), 771–787.

Bruhn, R. L., Sauber, J., Cotton, M. M., Pavlis, T. L., Burgess, E., Ruppert, N., & Forster, R. R. (2012). Plate margin deformation and active tectonics along the northern edge of the Yakutat Terrane in the Saint Elias Orogen, Alaska, and Yukon, Canada. *Geosphere*, *8*(6), 1384–1407.

Buscher, J. T., Berger, A. L., & Spotila, J. A. (2008). Exhumation in the Chugach–Kenai Mountain belt above the Aleutian subduction zone, southern Alaska. *Washington DC American Geophysical Union Geophysical Monograph Series*, *179*, 151–166.

Calvert, A. J., Bostock, M. G., Savard, G., & Unsworth, M. J. (2020). Cascadia low frequency earthquakes at the base of an overpressured subduction shear zone. *Nature Communications*, *11*(1), 3874. http://dx.doi.org/10.1038/s41467-020-17609-3

Chapman, J. B., Pavlis, T. L., Bruhn, R. L., Worthington, L. L., Gulick, S. P., & Berger, A. L. (2012). Structural relationships in the eastern syntaxis of the St. Elias orogen, Alaska. *Geosphere*, *8*(1), 105–126.

Christeson, G. L., Gulick, S. P., van Avendonk, H. J., Worthington, L. L., Reece, R. S., & Pavlis, T. L. (2010). The Yakutat terrane: Dramatic change in crustal thickness across the transition fault, Alaska. *Geology*, *38*(10), 895–898.

Christeson, G. L., Van Avendonk, H. J. A., Gulick, S. P. S., Reece, R. S., Pavlis, G. L., & Pavlis, T. L. (2013). Moho interface beneath Yakutat terrane, southern Alaska. *Journal of Geophysical Research: Solid Earth*, *118*(9), 5084–5097.

Clark, S. H. B. (1973). The McHugh complex of south-central Alaska. U.S. *Geological Survey Bulletin*, *1372-D*, D1–D11.

Cowan, D. S. (2003). Revisiting the Baranof–Leech River hypothesis for early Tertiary coastwise transport of the Chugach–Prince William Terrane. *Earth and Planetary Science Letters*, *213*(3–4), 463–475.

Cunningham, E., & Lekić, V. (2019). Constraining crustal structure in the presence of sediment: A multiple converted wave approach. *Geophysical Journal International*, *219*(1), 313–327. http://dx.doi.org/10.1093/gji/ggz298

Daly, K. A., Abers, G. A., Mann, M. E., Roecker, S., & Christensen, D. H. (2021). Subduction of an oceanic plateau across southcentral Alaska: High-resolution seismicity. *Journal of Geophysical Research: Solid Earth*, *126*(11). http://dx.doi.org/10.1029/2021JB022809

Davidson, C., & Garver, J. I. (2017). Age and origin of the resurrection ophiolite and associated turbidites of the Chugach–Prince William Terrane, Kenai Peninsula, Alaska. *The Journal of Geology*, *125*(6), 681–700.

Eberhart-Phillips, D., Christensen, D. J., Brocher, T. M., Hansen, R., Ruppert, N. A., Haeussler, P. J., & Abers, G. A. (2006). Imaging the transition from Aleutian subduction to Yakutat collision in central Alaska, with local earthquakes and active source data. *Journal of Geophysical Research*, *111*, B11303. http://dx.doi.org/10.1029/2005JB004240

Enkelmann, E., Garver, J. I., & Pavlis, T. L. (2008). Rapid exhumation of ice-covered rocks of the Chugach–St. Elias orogen, Southeast Alaska. *Geology*, *36*(12), 915–918.

Enkelmann, E., Koons, P. O., Pavlis, T. L., Hallet, B., Barker, A., Elliott, J., et al. (2015a). Cooperation among tectonic and surface processes in the St. Elias Range, Earth's highest coastal mountains. *Geophysical Research Letters*, *42*(14), 5838–5846.

Enkelmann, E., Valla, P. G., & Champagnac, J. D. (2015b). Low-temperature thermochronology of the Yakutat plate corner, St. Elias Range (Alaska): Bridging short-term and long-term deformation. *Quaternary Science Reviews*, *113*, 23–38.

Enkelmann, E., Zeitler, P. K., Garver, J. I., Pavlis, T. L., & Hooks, B. P. (2010). The thermochronological record of tectonic and surface process interaction at the Yakutat–North American collision zone in southeast Alaska. *American Journal of Science*, *310*(4), 231–260.

Farra, V., & Vinnik, L. (2000). Upper mantle stratification by P and S receiver functions. *Geophysical Journal International*, *141*(3), 699–712. https://doi.org/10.1046/j.1365-246x.2000.00118.x

Feng, L., & Ritzwoller, M. H. (2019). A 3-D shear velocity model of the crust and uppermost mantle beneath Alaska including apparent radial anisotropy. *Journal of Geophysical Research: Solid Earth*, *124*(10), 10468–10497. http://dx.doi.org/10.1029/2019JB018122

Ferris, A., Abers, G. A., Christensen, D. H., & Veenstra, E. (2003). High resolution image of the subducted Pacific (?) plate beneath central Alaska, 50–150 km depth. *Earth and Planetary Science Letters*, *214*(3–4), 575–588. http://dx.doi.org/10.1016/S0012-821X(03)00403-5

Fisher, M. A., & Magoon, L. B. (1978). Geologic framework of lower cook inlet, Alaska. *AAPG Bulletin*, *62*(3), 373–402.

Fisher, M. A., von Huene, R., Smith, G. L., & Bruns, T. R. (1983). Possible seismic reflections from the downgoing Pacific plate, 275 kilometers arcward from the eastern Aleutian trench. *Journal of Geophysical Research: Solid Earth*, *88*(B7), 5835–5849. http://dx.doi.org/10.1029/JB088iB07p05835

Freeland, G. L., & Dietz, R. S. (1973). Rotation history of Alaskan tectonic blocks. *Tectonophysics*, *18*(3–4), 379–389.

Fuis, G. S., Ambos, E. L., Mooney, W. D., Christensen, N. I., & Geist, E. (1991). Crustal structure of accreted terranes in southern Alaska, Chugach Mountains and Copper River basin, from seismic refraction results. *Journal of Geophysical Research: Solid Earth*, *96*(B3), 4187–4227. http://dx.doi.org/10.1029/90JB02316

Fuis, G. S., Moore, T. E., Plafker, G., Brocher, T. M., Fisher, M. A., Mooney, W. D., et al. (2008). Trans-Alaska crustal transect and continental evolution involving subduction underplating and synchronous foreland thrusting. *Geology*, *36*(3), 267. http://dx.doi.org/10.1130/G24257A.1

Fuis, G. S., & Plafker, G. (1991). Evolution of deep structure along the trans-Alaska crustal transect, Chugach Mountains and Copper River basin, southern Alaska. *Journal of Geophysical Research: Solid Earth*, *96*(B3), 4229–4253. http://dx.doi.org/10.1029/90JB02276

Gama, I., Fischer, K. M., Dalton, C. A., & Eilon, Z. (2022b). Variations in lithospheric thickness across the Denali fault and in northern Alaska. *Geophysical Research Letters*, *49*(24). http://dx.doi.org/10.1029/2022GL101256

Gama, I., Fischer, K. M., & Hua, J. (2022a). Mapping the lithosphere and asthenosphere beneath Alaska with Sp converted waves. *Geochemistry, Geophysics, Geosystems*, *23*(10). http://dx.doi.org/10.1029/2022GC010517

Garver, J. I., & Davidson, C. M. (2015). Southwestern Laurentian zircons in upper cretaceous flysch of the Chugach–Prince William Terrane in Alaska. *American Journal of Science*, *315*(6), 537–556.

Goodwin, E. B., Fuis, G. S., Nokleberg, W. J., & Ambos, E. L. (1989). The crustal structure of the Wrangellia terrane along the east Glenn highway, eastern-southern Alaska. *Journal*

of Geophysical Research: Solid Earth, *94*(B11), 16037–16057. http://dx.doi.org/10.1029/JB094iB11p16037

Greene, A. R., Scoates, J. S., Weis, D., Katvala, E. C., Israel, S., & Nixon, G. T. (2010). The architecture of oceanic plateaus revealed by the volcanic stratigraphy of the accreted Wrangellia oceanic plateau. *Geosphere*, *6*(1), 47–73.

Gulick, S. P., Lowe, L. A., Pavlis, T. L., Gardner, J. V., & Mayer, L. A. (2007). Geophysical insights into the transition fault debate: Propagating strike slip in response to stalling Yakutat block subduction in the Gulf of Alaska. *Geology*, *35*(8), 763–766.

Hales, A. L., & Asada, T. (1966). Crustal structure in coastal Alaska. In J. S. Steinhart & T. J. Smith (Eds.), *Geophysical Monograph Series* (pp. 420–432). Washington, DC: American Geophysical Union. http://dx.doi.org/10.1029/GM010p0420

Haney, M. M., Ward, K. M., Tsai, V. C., & Schmandt, B. (2020). Bulk structure of the crust and upper mantle beneath Alaska from an approximate Rayleigh-wave dispersion formula. *Seismological Research Letters*, *91*(6), 3064–3075. http://dx.doi.org/10.1785/0220200162

Hansen, S. M., & Schmandt, B. (2017). P and S wave receiver function imaging of subduction with scattering kernels. *Geochemistry, Geophysics, Geosystems*, *18*(12), 4487–4502.

Hopper, E., Fischer, K. M., Wagner, L. S., & Hawman, R. B. (2017). Reconstructing the end of the Appalachian orogeny. *Geology*, *45*(1), 15–18. http://dx.doi.org/10.1130/G38453.1

Hua, J., Fischer, K. M., Mancinelli, N. J., & Bao, T. (2020b). Imaging with pre-stack migration based on Sp scattering kernels. *Geophysical Journal International*, *220*, 428–449. http://dx.doi.org/10.1093/gji/ggz459

Hua, J., Fischer, K. M., Wu, M., & Blom, N. A. (2020a). New approaches to multifrequency *Sp* stacking tested in the Anatolian region. *Journal of Geophysical Research: Solid Earth*, *125*(11). http://dx.doi.org/10.1029/2020JB020313

Hyndman, R. D., & Peacock, S. M. (2003). Serpentinization of the forearc mantle. *Earth and Planetary Science Letters*, *212*(3–4), 417–432. http://dx.doi.org/10.1016/S0012-821X(03)00263-2

Jadamec, M. A. (2016). Insights on slab-driven mantle flow from advances in three-dimensional modelling. *Journal of Geodynamics*, *100*, 51–70.

Jadamec, M. A., & Billen, M. I. (2010). Reconciling surface plate motions with rapid three-dimensional mantle flow around a slab edge. *Nature*, *465*(7296), 338–341. http://dx.doi.org/10.1038/nature09053

Jadamec, M. A., & Billen, M. I. (2012). The role of rheology and slab shape on rapid mantle flow: Three-dimensional numerical models of the Alaska slab edge. *Journal of Geophysical Research: Solid Earth*, *117*(B2).

Jadamec, M. A., Billen, M. I., & Roeske, S. M. (2013). Three-dimensional numerical models of flat slab subduction and the Denali fault driving deformation in south-central Alaska. *Earth and Planetary Science Letters*, *376*, 29–42.

Kawakatsu, H., Kumar, P., Takei, Y., Shinohara, M., Kanazawa, T., Araki, E., & Suyehiro, K. (2009). Seismic evidence for sharp lithosphere-asthenosphere boundaries of oceanic plates. *Science*, *324*(5926), 499–502.

Kennett, B. L. N. (1991). The removal of free surface interactions from three-component seismograms. *Geophysical Journal International*, *104*(1), 153–154. http://dx.doi.org/10.1111/j.1365-246X.1991.tb02501.x

Kennett, B. L. N., Engdahl, E. R., & Buland, R. (1995). Constraints on seismic velocities in the Earth from travel times. *Geophysical Journal International*, *122*(1), 108–124. http://dx.doi.org/10.1111/j.1365-246X.1995.tb03540.x

Kim, Y., Abers, G. A., Li, J., Christensen, D., Calkins, J., & Rondenay, S. (2014). Alaska Megathrust 2: Imaging the megathrust zone and Yakutat/Pacific plate interface in the Alaska subduction zone. *Journal of Geophysical Research: Solid Earth*, *119*(3), 1924–1941. http://dx.doi.org/10.1002/2013JB010581

Kim, D., Keranen, K. M., Abers, G. A., & Brown, L. D. (2019). Enhanced resolution of the subducting plate interface in Central Alaska from autocorrelation of local earthquake coda. *Journal of Geophysical Research: Solid Earth*, *124*(2), 1583–1600. http://dx.doi.org/10.1029/2018JB016167

Király, A., Portner, D. E., Haynie, K. L., Chilson-Parks, B. H., Ghosh, T., Jadamec, M., et al. (2020). The effect of slab gaps on subduction dynamics and mantle upwelling. *Tectonophysics*, *785*, 228458.

Koons, P. O., Hooks, B. P., Pavlis, T., Upton, P., & Barker, A. D. (2010). Three-dimensional mechanics of Yakutat convergence in the southern Alaskan plate corner. *Tectonics*, *29*(4).

Korja, A., & Heikkinen, P. J. (2008). *Seismic images of paleoproterozoic microplate boundaries in the Fennoscandian Shield*. Special Paper 440: When Did Plate Tectonics Begin on Planet Earth? (Vol. *440*, pp. 229–248). Geological Society of America. http://dx.doi.org/10.1130/2008.2440(11)

Krueger, H. E., Gama, I., & Fischer, K. M. (2021). Global patterns in Cratonic mid-lithospheric discontinuities from Sp receiver functions. *Geochemistry, Geophysics, Geosystems*, *22*(6). http://dx.doi.org/10.1029/2021GC009819

Kumar, P., & Kawakatsu, H. (2011). Imaging the seismic lithosphere-asthenosphere boundary of the oceanic plate: Oceanic lab imaging. *Geochemistry, Geophysics, Geosystems*, *12*(1). http://dx.doi.org/10.1029/2010GC003358

Kusky, T. M., Glass, A., & Bradley, D. C. (2007). Structure, Cr-chemistry, and age of the Border Ranges ultramafic/mafic complex: A suprasubductionzone ophiolite complex. In K. D. Ridgway, J. Trop, M. Glen, & J. M. O'Neill (Eds.), *Tectonic growth of a collisional continental margin: Crustal evolution of southern Alaska* (Vol. *431*, pp. 207–225). Geological Society of America, Special Papers.

Langston, C. A. (1977). Corvallis, Oregon, crustal and upper mantle receiver structure from teleseismic *P* and *S* waves. *Bulletin of the Seismological Society of America*, *67*(3), 713–724. http://dx.doi.org/10.1785/BSSA0670030713

Lekić, V., & Fischer, K. M. (2017). Interpreting spatially stacked Sp receiver functions. *Geophysical Journal International*, *210*(2), 874–886.

Lekić, V., French, S. W., & Fischer, K. M. (2011). Lithospheric thinning beneath rifted regions of Southern California. *Science*, *334*(6057), 783–787. http://dx.doi.org/10.1126/science.1208898

Li, C., Gao, H., & Williams, M. L. (2020). Seismic characteristics of the eastern north American crust with Ps converted waves: Terrane accretion and modification of continental crust. *Journal of Geophysical Research: Solid Earth*, *125*, e2019JB018727. http://dx.doi.org/10.1029/2019JB018727

Li, J., Abers, G. A., Kim, Y., & Christensen, D. (2013). Alaska megathrust 1: Seismicity 43 years after the great 1964 Alaska megathrust earthquake. *Journal of Geophysical Research: Solid Earth*, *118*(9), 4861–4871. http://dx.doi.org/10.1002/jgrb.50358

Long, M. D., Benoit, M. H., Aragon, J. C., & King, S. D. (2019). Seismic imaging of mid-crustal structure beneath central and eastern North America: Possibly the elusive Grenville deformation? *Geology*, *47*(4), 371–374.

MacKevett, E. M., & Plafker, G. (1974). The border ranges fault in south-central Alaska. *US Geological Survey Journal of Research*, *2*, 323–329.

Malik, A. M. (2019). U-Pb dating of detrital zircon from turbidites of the Chugach and Prince William Terranes, Alaska: Implications for the significance of the Contact fault system as a terrane boundary. *Proceedings of the Keck Geology Consortium*, *32*.

Mancinelli, N. J., & Fischer, K. M. (2017). The spatial sensitivity of Sp converted waves – Scattered wave kernels and their applications to receiver-function migration and inversion. *Geophysical Journal International*, *212*, 1722–1735. http://dx.doi.org/10.1093/gji/ggx506

Mankhemthong, N., Doser, D. I., & Pavlis, T. L. (2013). Interpretation of gravity and magnetic data and development of two-dimensional cross-sectional models for the border ranges fault system, south-central Alaska. *Geosphere*, *9*(2), 242–259. http://dx.doi.org/10.1130/GES00833.1

Mann, M. E., Abers, G. A., Daly, K. A., & Christensen, D. H. (2022). Subduction of an oceanic plateau across southcentral Alaska: Scattered-wave imaging. *Journal of Geophysical Research: Solid Earth*, *127*(1). http://dx.doi.org/10.1029/2021JB022697

Martin-Short, R., Allen, R., Bastow, I. D., Porritt, R. W., & Miller, M. S. (2018). Seismic imaging of the Alaska subduction zone: Implications for slab geometry and volcanism. *Geochemistry, Geophysics, Geosystems*, *19*(11), 4541–4560. http://dx.doi.org/10.1029/2018GC007962

Miller, M. S., O'Driscoll, L. J., Porritt, R. W., & Roeske, S. M. (2018). Multiscale crustal architecture of Alaska inferred from P receiver functions. *Lithosphere*, *10*(267–278), 1050. http://dx.doi.org/10.1130/L701.1

Motyka, R. J., Poreda, R. J., & Jeffrey, A. W. (1989). Geochemistry, isotopic composition, and origin of fluids emanating from mud volcanoes in the Copper River basin, Alaska. *Geochimica et Cosmochimica Acta*, *53*(1), 29–41.

Newell, D. L., Benowitz, J. A., Regen, S. P., & Hiett, C. D. (2023). Roadblocks and speed limits: Mantle-to-surface volatile flux through the lithospheric-scale Denali fault, Alaska. *Geology*, *51*, 576–580. http://dx.doi.org/10.1130/G51068.1

Nilsen, T. H., & Zuffa, G. G. (1982). The Chugach terrane, a cretaceous trench-fill deposit, southern Alaska. *Geological Society, London, Special Publications*, *10*(1), 213–227.

Nokleberg, W. J., Jones, D. L., & Silberling, N. J. (1985). Origin and tectonic evolution of the Maclaren and Wrangellia terranes, eastern Alaska Range, Alaska. *Geological Society of America Bulletin*, *96*(10), 1251. http://dx.doi.org/10.1130/0016-7606(1985)96%3c1251:OATEOT%3e2.0.CO;2

Nokleberg, W. J., Foster, H. L., & Aleinikoff, J. N. (1989). Geology of the northern Copper River basin, eastern Alaska range, and southern Yukon-Tanana Upland. In W. J. Nokleberg & M. A. Fisher (Eds.), *Alaskan geological and geophysical transect* (pp. 34–63). Washington, DC: American Geophysical Union. http://dx.doi.org/10.1029/FT104p0034

Pavlis, T. L. (1982). Origin and age of the border ranges fault of southern Alaska and its bearing on the late Mesozoic tectonic evolution of Alaska. *Tectonics*, *1*(4), 343–368.

Pavlis, T. L., Amato, J. M., Trop, J. M., Ridgway, K. D., Roeske, S. M., & Gehrels, G. E. (2019). Subduction polarity in ancient arcs: A call to integrate geology and geophysics to decipher the Mesozoic tectonic history of the northern cordillera of North America. *GSA Today*, *29*(11). http://dx.doi.org/10.1130/GSATG402A.1

Pavlis, T. L., Chapman, J. B., Bruhn, R. L., Ridgway, K., Worthington, L. L., Gulick, S. P., & Spotila, J. (2012). Structure of the actively deforming fold-thrust belt of the St. Elias orogen with implications for glacial exhumation and three-dimensional tectonic processes. *Geosphere*, *8*(5), 991–1019.

Pavlis, T. L., Picornell, C., Serpa, L., Bruhn, R. L., & Plafker, G. (2004). Tectonic processes during oblique collision: Insights from the St. Elias orogen, northern north American Cordillera. *Tectonics*, *23*(3).

Pavlis, T. L., & Roeske, S. M. (2007). The Border Ranges fault system, southern Alaska. In *Special Paper 431: tectonic growth of a collisional continental margin: Crustal evolution of southern Alaska* (Vol. *431*, pp. 95–127). Geological Society of America. http://dx.doi.org/10.1130/2007.2431(05)

Peacock, S. M., Christensen, N. I., Bostock, M. G., & Audet, P. (2011). High pore pressures and porosity at 35 km depth in the Cascadia subduction zone. *Geology*, *39*(5), 471–474. http://dx.doi.org/10.1130/G31649.1

Plafker, G., & Berg, H. C. (1994). *Overview of the geology and tectonic evolution of Alaska* (pp. 989–1021). The Geology of North America, GSA, Chapter 33.

Plafker, G., Nokleberg, W. J., & Lull, J. S. (1989). Bedrock geology and tectonic evolution of the Wrangellia, eninsular, and Chugach Terranes along the Trans-Alaska Crustal Transect in the Chugach Mountains and Southern Copper River Basin, Alaska. *Journal of Geophysical Research: Solid Earth*, *94*(B4), 4255–4295.

Powell, D., & Amoco Oil Co. (2019). *Geological report to the Ahtna Corporation, Copper River basin, Alaska, 1975*. Alaska Division of Geological & Geophysical Surveys. Geologic Materials Center Data Report 455, 26 p., 9 sheets. https://doi.org/10.14509/30324

Reiners, P. W., & Brandon, M. T. (2006). Using thermochronology to understand orogenic erosion. *Annual Review of Earth and Planetary Sciences*, *34*, 419–466.

Richter, D. H., Smith, J. G., Lanphere, M. A., Dalrymple, G. B., Reed, B. L., & Shew, N. (1990). Age and progression of volcanism, Wrangell volcanic field, Alaska. *Bulletin of Volcanology*, *53*, 29–44.

Ridgway, K. D., Trop, J. M., Nokleberg, W. J., Davidson, C. M., & Eastham, K. R. (2002). Mesozoic and Cenozoic tectonics of the eastern and central Alaska range: Progressive basin development and deformation in a suture zone. *Geological Society of America Bulletin*, *114*(12), 1480–1504.

Rondenay, S. (2009). Upper mantle imaging with array recordings of converted and scattered teleseismic waves. *Surveys in Geophysics*, *30*(4–5, 405), 377. http://dx.doi.org/10.1007/s10712-009-9071-5

Rondenay, S., Abers, G. A., & van Keken, P. E. (2008). Seismic imaging of subduction zone metamorphism. *Geology*, *36*(4), 275. http://dx.doi.org/10.1130/G24112A.1

Rossi, G., Abers, G. A., Rondenay, S., & Christensen, D. H. (2006). Unusual mantle Poisson's ratio, subduction, and crustal structure in central Alaska. *Journal of Geophysical Research*, *111*(B9), B09311. http://dx.doi.org/10.1029/2005JB003956

Sato, H., Kato, N., Abe, S., Van Horne, A., & Takeda, T. (2015). Reactivation of an old plate interface as a strike-slip fault in a slip-partitioned system: Median tectonic line, SW Japan. *Tectonophysics*, *644–645*, 58–67. http://dx.doi.org/10.1016/j.tecto.2014.12.020

Schartman, A., Enkelmann, E., Garver, J. I., & Davidson, C. M. (2019). Uplift and exhumation of the Russell fiord and boundary blocks along the northern Fairweather transform fault, Alaska. *Lithosphere*, *11*(2), 232–251.

Sheehan, A. F., Abers, G. A., Jones, C. H., & Lerner-Lam, A. L. (1995). Crustal thickness variations across the Colorado Rocky Mountains from teleseismic receiver functions. *Journal of Geophysical Research: Solid Earth*, *100*(B10), 20391–20404. http://dx.doi.org/10.1029/95JB01966

Shellenbaum, D. P., L. S. Gregersen, & P. R. Delaney (2010). *Top Mesozoic unconformity depth map of the Cook Inlet basin, Alaska*. Rept. Investig. 2010-2, Alaska Division of Geological and Geophysical Surveys, Fairbanks, Alaska.

Smart, K. J., Pavlis, T. L., Sisson, V. B., Roeske, S. M., & Snee, L. W. (1996). The border ranges fault system in Glacier Bay National Park, Alaska: Evidence for major early Cenozoic dextral strike-slip motion. *Canadian Journal of Earth Sciences*, *33*(9), 1268–1282.

Smith, K., & Tape, C. (2020). Seismic response of cook inlet Sedimentary Basin, Southern Alaska. *Seismological Research Letters*, *91*(1), 33–55. http://dx.doi.org/10.1785/0220190205

Spotila, J. A., & Berger, A. L. (2010). Exhumation at orogenic indentor corners under long-term glacial conditions: Example of the St. Elias orogen, southern Alaska. *Tectonophysics*, *490*(3–4), 241–256.

Stephens, C. D., Page, R. A., & Lahr, J. C. (1990). Reflected and mode-converted seismic waves within the shallow Aleutian Subduction Zone, Southern Kenai Peninsula, Alaska. *Journal of Geophysical Research*, *95*(B5), 6883. http://dx.doi.org/10.1029/JB095iB05p06883

Tape, C., Christensen, D., Moore-Driskell, M. M., Sweet, J., & Smith, K. (2017). Southern Alaska lithosphere and mantle observation network (SALMON): A seismic experiment covering the active arc by road, boat, plane, and helicopter. *Seismological Research Letters*, *88*(4), 1185–1202. http://dx.doi.org/10.1785/0220160229

Terhune, P. J., Benowitz, J. A., Trop, J. M., O'Sullivan, P. B., Gillis, R. J., & Freymueller, J. T. (2019). Cenozoic tectono-thermal history of the southern Talkeetna Mountains, Alaska: Insights into a potentially alternating convergent and transform plate margin. *Geosphere*, *15*(5), 1539–1576.

Tikoff, B., Housen, B. A., Maxson, J. A., Nelson, E. M., Trevino, S., & Shipley, T. F. (2023). Hit-and-run model for Cretaceous–Paleogene tectonism along the western margin of Laurentia. In S. J. Whitmeyer, M. L. Williams, D. A. Kellett, & B. Tikoff (Eds.), *Laurentia: Turning points in the evolution of a continent* (pp. 659–705). Geological Society of America. http://dx.doi.org/10.1130/2022.1220(32)

Trop, J. M., Benowitz, J., Cole, R. B., & O'Sullivan, P. (2019). Cretaceous to Miocene magmatism, sedimentation, and exhumation within the Alaska Range suture zone: A polyphase reactivated terrane boundary. *Geosphere*, *15*(4), 1066–1101.

Trop, J. M., Benowitz, J. A., Kirby, C. S., & Brueseke, M. E. (2022). Geochronology of the Wrangell Arc: Spatial-temporal evolution of slab-edge magmatism along a flat-slab, subduction-transform transition, Alaska-Yukon. *Geosphere*, *18*(1), 19–48.

Trop, J. M., Benowitz, J. A., Koepp, D. Q., Sunderlin, D., Brueseke, M. E., Layer, P. W., & Fitzgerald, P. G. (2020). Stitch in the ditch: Nutzotin Mountains (Alaska) fluvial strata and a dike record ca. 117–114 Ma accretion of Wrangellia with western North America and initiation of the Totschunda fault. *Geosphere*, *16*(1), 82–110.

Trop, J. M., & Ridgway, K. D. (2007). Mesozoic and Cenozoic tectonic growth of southern Alaska: A sedimentary basin perspective. In *Special paper 431: Tectonic growth of a collisional continental margin: Crustal evolution of southern Alaska* (Vol. *431*, pp. 55–94). Geological Society of America. http://dx.doi.org/10.1130/2007.2431(04)

Valentino, J. D., Spotila, J. A., Owen, L. A., & Buscher, J. T. (2016). Rock uplift at the transition from flat-slab to normal subduction: The Kenai Mountains, Southeast Alaska. *Tectonophysics*, *671*, 63–75. http://dx.doi.org/10.1016/j.tecto.2016.01.022

Veenstra, E., Christensen, D. H., Abers, G. A., & Ferris, A. (2006). Crustal thickness variation in south-central Alaska. *Geology*, *34*(9), 781. http://dx.doi.org/10.1130/G22615.1

Ward, K. M., & Lin, F. (2018). Lithospheric structure across the Alaskan cordillera from the joint inversion of surface waves and receiver functions. *Journal of Geophysical Research: Solid Earth*, *123*(10), 8780–8797. http://dx.doi.org/10.1029/2018JB015967

Worthington, L. L., Van Avendonk, H. J., Gulick, S. P., Christeson, G. L., & Pavlis, T. L. (2012). Crustal structure

of the Yakutat terrane and the evolution of subduction and collision in southern Alaska. *Journal of Geophysical Research: Solid Earth*, *117*(B1).

Ye, S., Flueh, E. R., Klaeschen, D., & Huene, R. (1997). Crustal structure along the EDGE transect beneath the Kodiak shelf off Alaska derived from OBH seismic refraction data. *Geophysical Journal International*, *130*(2), 283–302. http://dx.doi.org/10.1111/j.1365-246X.1997.tb05648.x

Zhang, Y., Li, A., & Hu, H. (2019). Crustal structure in Alaska from receiver function analysis. *Geophysical Research Letters*, *46*, 1284–1292. http://dx.doi.org/10.1029/2018GL081011